ACS APPLIED MATERIALS & INTERFACES

Research Article

www.acsami.org

Broadband Epsilon-near-Zero Reflectors Enhance the Quantum Efficiency of Thin Solar Cells at Visible and Infrared Wavelengths

A. J. Labelle,[†,‡] M. Bonifazi,[‡,§] Y. Tian,[‡,§] C. Wong,[†] S. Hoogland,[†] G. Favraud,[§] G. Walters,[†] B. Sutherland,[†] M. Liu,[†] Jun Li,[∥] Xixiang Zhang,[⊥] S. O. Kelley,[∥,#] E. H. Sargent,[*,†] and A. Fratalocchi[*,§]

[†]Department of Electrical and Computer Engineering, University of Toronto, 10 Kings College Road, Toronto, Ontario M5S 3G4, Canada

[§]PRIMALIGHT, Faculty of Electrical Engineering, and [⊥]PRIMALIGHT, Faculty of Physical Sciences and Engineering, King Abdullah University of Science and Technology (KAUST), Thuwal 23955-6900, Saudi Arabia

[∥]Department of Pharmaceutical Sciences and [#]Department of Biochemistry, Faculty of Medicine, University of Toronto, Toronto, Ontario M5S 3M2, Canada

Supporting Information

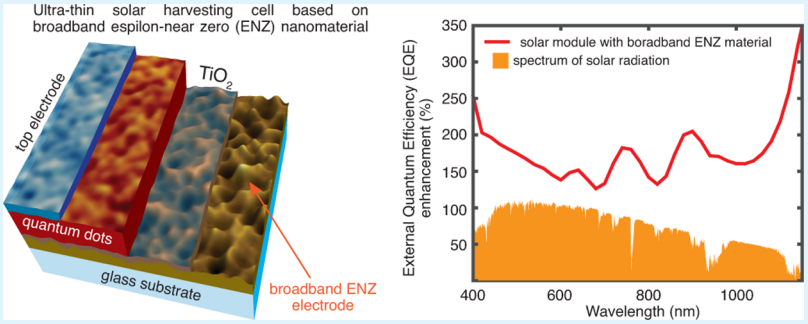

ABSTRACT: The engineering of broadband absorbers to harvest white light in thin-film semiconductors is a major challenge in developing renewable materials for energy harvesting. Many solution-processed materials with high manufacturability and low cost, such as semiconductor quantum dots, require the use of film structures with thicknesses on the order of 1 μm to absorb incoming photons completely. The electron transport lengths in these media, however, are 1 order of magnitude smaller than this length, hampering further progress with this platform. Herein, we show that, by engineering suitably disordered nanoplasmonic structures, we have created a new class of dispersionless epsilon-near-zero composite materials that efficiently harness white light. Our nanostructures localize light in the dielectric region outside the epsilon-near-zero material with characteristic lengths of 10−100 nm, resulting in an efficient system for harvesting broadband light when a thin absorptive film is deposited on top of the structure. By using a combination of theory and experiments, we demonstrate that ultrathin layers down to 50 nm of colloidal quantum dots deposited atop the epsilon-near-zero material show an increase in broadband absorption ranging from 200% to 500% compared to a planar structure of the same colloidal quantum-dot-absorber average thickness. When the epsilon-near-zero nanostructures were used in an energy-harvesting module, we observed a spectrally averaged 170% broadband increase in the external quantum efficiency of the device, measured at wavelengths between 400 and 1200 nm. Atomic force microscopy and photoluminescence excitation measurements demonstrate that the properties of these epsilon-near-zero structures apply to general metals and could be used to enhance the near-field absorption of semiconductor structures more widely. We have developed an inexpensive electrochemical deposition process that enables scaled-up production of this nanomaterial for large-scale energy-harvesting applications.

KEYWORDS: *colloidal quantum dots, nanophotonics, epsilon-near-zero materials, solar energy harvesting, atomic force microscopy, electron energy loss spectroscopy*

INTRODUCTION

Colloidal quantum dot (CQD) materials are used in a wide array of light-harvesting systems including photodetectors,[1−4] photovoltaics,[5−10] and photojunction field-effect transistor devices.[11] The attractive characteristics of these materials include low costs of fabrication, low materials utilization, and size-tunable optical band gaps. Combined, these features allow for control of the spectral response over a wide range within a low-cost platform.[12]

Further progress in this promising system is hampered by a compromise between light absorption and charge-carrier

Received: October 29, 2016
Accepted: January 18, 2017
Published: February 3, 2017

DOI: 10.1021/acsami.6b13713
ACS Appl. Mater. Interfaces 2017, 9, 5556−5565

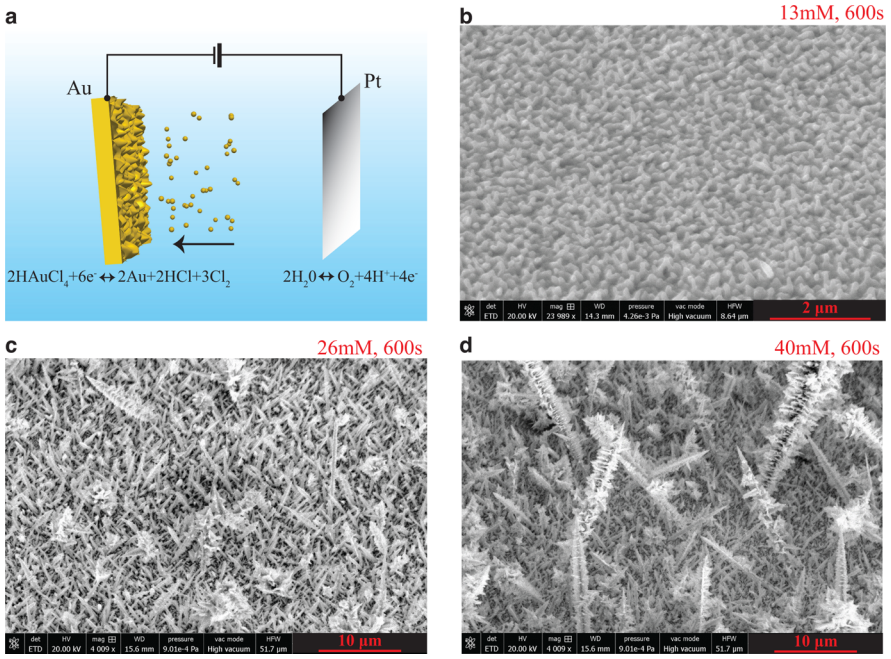

Figure 1. Fabrication of broadband ENZ materials by the electrodeposition of Au nanostructures. (a) Redox reaction illustrating the concepts behind the electrodeposition of nanostructured Au films. (b–d) Top-view SEM images of nanostructured Au electrodes prepared at an applied bias of 250 mV for an exposure time of 10 min using $HAuCl_4$ solution concentrations of (b) 13, (c) 26, and (d) 40 mM.

extraction: Transport lengths today are limited to ~400 nm,[12] but more than 1 μm of planar material is required to absorb all impinging solar photons with wavelengths greater than 800 nm. Numerous strategies have been implemented to address this issue, including reducing the collection distance using heterojunctions[7,13−15] and coupling light into active films using substrate structuring techniques for increased absorption.[16,17] Plasmonic nanostructures have also been explored.[18−21] However, most of the electromagnetic energy is typically localized inside the metal, and only a small portion reaches the CQD film.[22]

Each of these technologies typically enhances the absorption of the semiconductor in a narrow spectral region. A major challenge is to conceive a material able to capture all incoming photons with energies above the band gap of 1.1 eV, the prerequisite band gap to approach the 30% thermodynamic limit of efficiency for single-junction solar cells.[23] If a medium with such a broadband response can be engineered, it could potentially open the realization of new generations of photovoltaic devices.

Herein we propose a novel strategy that makes use of epsilon-near-zero (ENZ) electromagnetic materials. The study of these systems is of considerable interest because of phenomena that occur when the refractive index of an optical medium reaches zero.[24−26] When light propagates into an ENZ material, the phase velocity of the wave diverges, and the energy velocity tends to zero, implying the formation of standing waves with infinite wavelength. An ENZ nanomaterial with a broad spectral response could slow down electromagnetic waves on scales much smaller than the charge diffusion length, thereby enabling the design of a new class of thin structures for efficient energy harvesting.

From an experimental perspective, the engineering of ENZ materials at optical wavelengths is quite challenging. To date, significant advances have been reported for specific frequency regions and light input conditions (angle of incidence and polarization);[25,26] as yet, however, the fabrication of ENZ structures whose operating wavelength spans the visible to the infrared region has not been achieved.

In this work, we design a new class of ultrabroadband ENZ materials by exploiting complex metallic structures. Pioneering investigations on complex optical systems reported various counterintuitive phenomena such as broadband energy harvesting, extreme light localization, photon condensation, and ultradark blackbody materials.[27−33] Herein, we illustrate the harnessing of these effects, turning a nanoplasmonic material into a complex network of dielectric ENZ nanostructures, connected by nanocavities with high dielectric permittivities. In previous reports, plasmonic strategies for absorption enhancement have often led to localization of light principally within the metal, making it difficult to extract energy in the desired light-harvesting-active semiconductor layer.[18] Our ENZ nanostructures, in contrast, efficiently localize white light within 10–100 nm outside the metal, creating a material with a record of broadband external quantum efficiency (EQE) enhancement when combined with thin absorptive films.

RESULTS AND DISCUSSION

Material Design and Characterization. We used electrodeposition[34−37] as a scalable fabrication process for assembling complex ENZ materials. Figure 1a presents a schematic view of the process. We used a three-probe potentiostat in a gold chloride ($HAuCl_4$) solution, with the reduction of gold (Au) atoms on the working electrode, which was itself coated with a thin planar Au film (see Materials and Methods for more details). Figure 1b–d shows scanning electron microscopy (SEM) images of samples prepared with exposure times of t = 10 min, using $HAuCl_4$ solutions of different concentrations. The fabricated samples were characterized by strongly disordered nanostructures, whose characteristic sizes spanned multiple spatial scales with features varying in the range between 10 nm and 1–2 μm. Multiscale disorder could be

DOI: 10.1021/acsami.6b13713
ACS Appl. Mater. Interfaces 2017, 9, 5556−5565

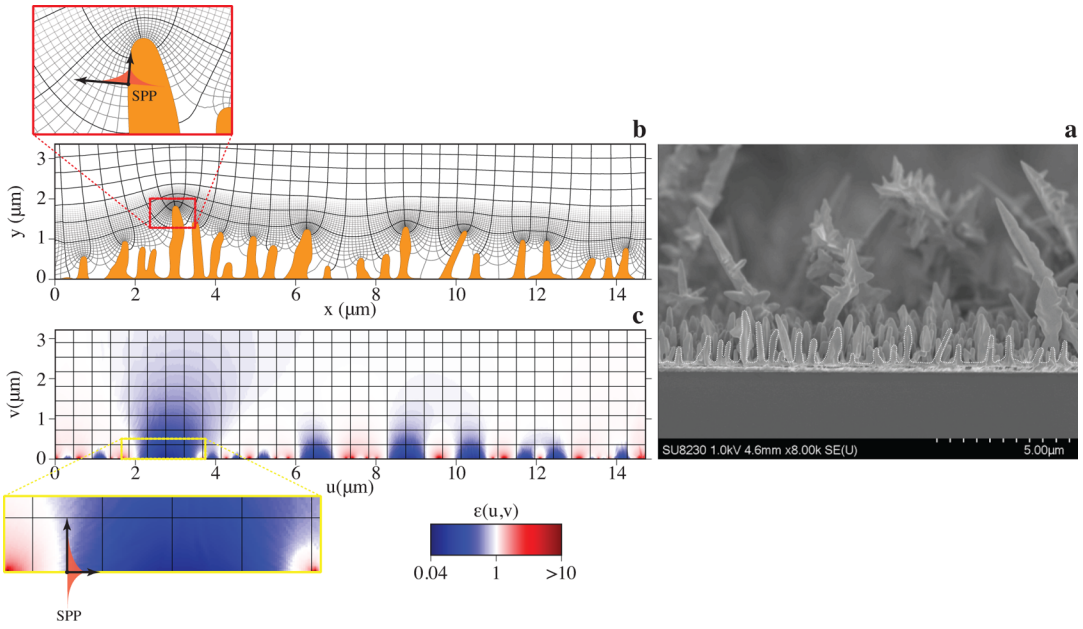

Figure 2. Formation of broadband ENZ materials in complex nanoplasmonic structures: theory. (a) SEM cross section of a nanostructured sample obtained at a $HAuCl_4$ concentration of 26 mM and a deposition time of t = 360 s. (b) Two-dimensional cross-sectional profile of the metallic surface. When light impinges on the structure, it excites the propagation of surface plasmon polariton (SPP) waves, which move along the complex surface of the metal (panel b, inset). This motion is conveniently described in a curvilinear grid (u, v), which conformally maps the metallic surface (panel b, gray grid). (c) In the transformed space (u, v), the SPP waves appear to propagate inside an inhomogeneous material with a dielectric permittivity $\epsilon(u,v)$ on the line at v = 0 (panel c, inset).

controlled by varying the solution concentration of $HAuCl_4$ (Figure 1b–d).

To characterize the optical response of the complex metal of Figure 1, we resorted to the transformation approach developed in ref 33. For the sake of simplicity and without loss of generality, here, we perform a two-dimensional analysis, which has the advantage of providing a clear physical description of the optical properties of the sample. A three-dimensional generalization requires very involved mathematics and is deferred to a future specialized work. Figure 2a shows an SEM cross section of a nanostructured material fabricated with a $HAuCl_4$ solution concentration of 26 mM and a deposition time of 360 s. Figure 2b illustrates a two-dimensional cross section of the metallic surface along the (x, y) plane. When light impinges on this structure, it excites surface plasmon polariton (SPP) waves,[38] which propagate on the metallic surface following its complex curvature (Figure 2b, inset). Because plasmon waves move on the surface of the sample, it is a natural choice to describe this motion on a reference system that is conformal with the metallic surface. An example of such conformal grid is shown by the gray axes of Figure 2b, which define a new set of coordinates (u, v). In the transformed space (u, v), the motion of surface plasmons is extremely simple and characterized by straight lines at v = 0 (Figure 2c and inset). In the coordinate space (u, v), the dynamics of light is described by the same set of Maxwell equations that model photon dynamics in the original (x, y) space, with the addition of a new inhomogeneous material with dielectric permittivity $\epsilon(u,v)$. This material takes into account the effects of the complex metallic surface of Figure 2b, whose geometry disappears in the flat space of Figure 2c. The calculation of the dielectric material $\epsilon(u,v)$ is performed with the standard arguments from transformation optics[39,40] (see Supporting Information and Figure S1). The approach we developed to calculate $\epsilon(u,v)$ is general and can be applied to arbitrary initial geometries in the (x, y) space. With the introduction of the transformed material $\epsilon(u,v)$, the two structures of Figure 2b,c—the complex metallic geometry in air (Figure 2b) and the flat metallic plane immersed in the inhomogeneous medium $\epsilon(u,v)$ (Figure 2c)—are exactly the same: Light does not experience any difference when propagating in one or the other.

The transformed medium of Figure 2c shows remarkable electromagnetic features. The variation of geometric curvature in Figure 2b generates a complex network of ENZ regions (Figure 2c, blue area) whose dielectric constant attains very low values of $\sim 10^{-3}$. ENZ regions are located outside the metal, in the semi-infinite plane for $v > 0$, and are separated by nanoscale areas of high dielectric constant $\epsilon > 10$ along the u axis. Figure S2 shows the spatial distribution of the transformed dielectric material $\epsilon[u(x,y),v(x,y)]$ in the original space (x, y), clarifying where the ENZ regions are created in space. As can be observed in the figure, the ENZ regions accumulate on the points of positive curvature of the metal near each nanostructured peak, whereas regions of high dielectric constant are created in the valleys of the metallic surface where the curvature changes sign. As the generation of ENZ nanostructures is of geometrical origin, ENZ regions are dispersionless and inherently insensitive to light input frequency. This is an exact result, as it is based on a transformation optics approach that does not rely on any approximations.[39] However, it is important to observe that the presence of a metal is fundamental for light to become strongly localized in the ENZ regions. If the metal is replaced by a different material that does not sustain surface polariton waves, in fact, light energy would simply penetrate the structure or be reflected, without experiencing any ENZ effect. We observed that the structure of Figure 2a,b cannot be modeled in the quasistatic approximation,[40] as this approach

DOI: 10.1021/acsami.6b13713
ACS Appl. Mater. Interfaces 2017, 9, 5556–5565

leads to $\epsilon(u,v) = 0$ throughout the transformed space, neglecting the essential contribution of ENZ regions.

Polychromatic Light Splitting in Complex ENZ Nanostructures. In the first series of experiments, we characterized the optical response of the ENZ material to broadband input light. Figure S3a–c shows the total absorption of the ENZ nanostructures when combined with an ultrathin (50-nm-thick) colloidal quantum dot film composed of 1.3 eV lead sulfide colloidal quantum dots (see Materials and Methods). Figure S3a shows a trend of increased absorption as a function of deposition time, in agreement with our theory that predicts the formation of an ENZ network with broadband absorption properties.

To quantitatively show that the absorption increase observed in our measurements is sustained by the ENZ network, we generated finite-difference time-domain (FDTD) models using the refractive index profile extracted from SEM images of fabricated samples (Figure 2a). In our simulations, we investigated the system response to different input wavelengths λ between λ = 450 nm and λ = 1100 nm. We solved a fully dispersive version of the Maxwell equations with our parallel FDTD code NANOCPP.[27,41] In our simulations, we considered the exact dispersion curve of gold taken from available experimental results[42] (Figure S4). Figure 3 (dashed lines) presents the results of this analysis, comparing theory and experiments for planar and disordered samples. We observed a broadband absorption increase throughout the visible and near-infrared region when a network of ENZ regions was formed. This comparison also demonstrates that the cross-sectional structure employed in Figure 3 is representative of the sample and can therefore be employed to investigate the light–matter interactions occurring in the material.

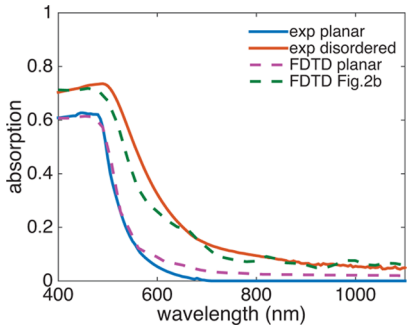

Figure 3. Broadband absorption of nanostructured electrodes: FDTD analysis and experiments. Comparison of the experimental (solid lines) and FDTD-calculated (dashed lines) absorption of planar and nanostructured samples obtained at t = 360 s with a 23 mM solution concentration of $HAuCl_4$. The FDTD analysis on nanostructured gold was carried out on the structure shown in Figure 2b.

Figure 4a provides more details on the behavior of ENZ nanostructures by illustrating the spatial distribution of the electromagnetic energy, $\mathcal{E}$, averaged over one optical cycle, when the system response reaches steady state. Figure 4a shows that light is split into polychromatic resonant states localized in different spatial regions of the metallic surface. Such complex light–matter interactions can be interpreted in the transformed space (u, v), which is presented in Figure 4b. To create a reference for the ENZ dielectric response, we combined Figure 4b with Figure 4c, which plots the corresponding inhomogeneous permittivity $\epsilon(u,v)$ of the ENZ material. By comparing panels b and c of Figure 4, one can clearly observe that polychromatic energy trapping is attained in each ENZ region. Movie M1 provides further details on the trapping process, showing the time evolution of the electromagnetic energy in the transformed domain (u, v). Once light impinges on the complex ENZ material, electromagnetic energy oscillates inside each ENZ region, eventually accumulating in the points of lowest refractive index. Each ENZ region acts as an effective cavity: During each round trip toward the cavity edges, electromagnetic waves are slowed down, and light energy becomes progressively trapped in the points of minimum wave velocity. To illustrate this process, we carried out an additional series of FDTD simulations by considering the elementary absorption unit of the system, which is illustrated in the inset of Figure 2c and is composed of an ENZ region sandwiched between two high-refractive-index regions on the top of a gold metal planar structure. The dielectric permittivities of the ENZ and the high-refractive-index regions are set to ϵ_r = 0.01 and ϵ_r = 7, respectively, and are considered dispersionless over the entire spectrum. Figure S5 presents FDTD results on the absorption of ENZ structures with different lengths L. The length L depends on the curvature of the metal in the original (x, y) space: The smaller the curvature, the higher the ENZ length L in the transformed space. FDTD-calculated spectra show that the absorption of each absorption unit of the system is not flat, with each ENZ layer localizing broadband light differently when the ENZ length is changed.

Enhanced Broadband Absorption in Thin Films. Figure 4a,b shows that ENZ regions that are sufficiently close to each other can interact electromagnetically, allowing energy to extend well beyond the metallic surface and create complex localized energy patterns on the 10–100-nm scale. When a film of absorptive material is placed in contact with these ENZ nanostructures, localized energy patterns provide a broadband energy reservoir for the film that can increase its absorption over a wide spectral range. In the next analysis, we investigated this process in more detail by using a combination of atomic force microscopy (AFM) imaging, photoconductive AFM (PC-AFM) imaging, and photoluminescence excitation (PLE) experiments.

Figure 5a,b presents AFM photocurrent images of two different zones of a nanostructured sample with a CQD film thickness of 50 nm. The photocurrent enhancement was measured by illuminating the sample with a laser of wavelength λ = 405 nm (see Materials and Methods). To analyze the spatial position of absorption enhancement, we superimposed the photocurrent enhancement on the surface profile of the nanostructured metal (Figure 5a,b, surface plot). To avoid the formation of electrical shorts between the AFM nanotip and the metal, we used a 10-nm layer of amorphous TiO_2, deposited on top of the metal by atomic layer deposition (ALD). The AFM measurements demonstrated that a significant photocurrent enhancement occurred in the metallic peaks of the nanostructures where the ENZ regions formed. This is further validated by Figure 6, which superimposes the AFM-retrieved photocurrent with the spatial distribution of ENZ regions, displaying an excellent one-to-one correspondence between peaks in the photocurrent (Figure 6a, maxima in the black solid line) and ENZ regions (Figure 6a, minima in the dashed blue line).

Figure S6 presents a comparative analysis between a peak (panels a and c) and a valley (panels b and d) of a sample composed of a nanostructured metal (t = 180 s, 13 mM solution) with no CQD film. This analysis allowed the ENZ

DOI: 10.1021/acsami.6b13713
ACS Appl. Mater. Interfaces 2017, 9, 5556–5565

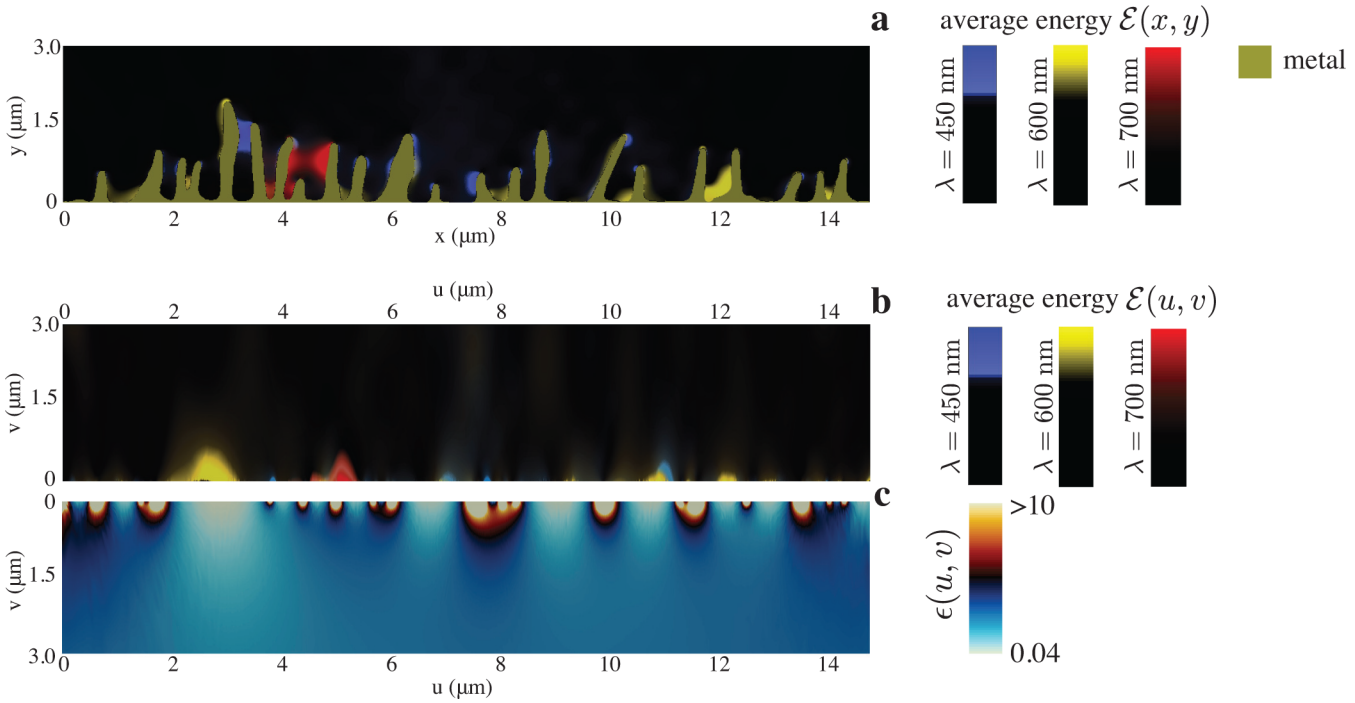

Figure 4. FDTD analysis of polychromatic light splitting in complex ENZ nanostructures. (a) Electromagnetic energy distribution $\mathcal{E}$, averaged over one optical cycle at steady state, upon illumination of the structure in Figure 2b by monochromatic light at different frequencies (λ = 450, 600, and 700 nm). To illustrate the effects of these excitations in a single plot, we used semitransparent color bars (panel a, right side) with shades of a given intensity of the excitation wavelength. The metallic structure is illustrated as a solid dark yellow area. (b) Energy distribution of panel a in the transformed space (u, v). (c) Distribution of dielectric permittivity $\epsilon(u,v)$ of the inhomogeneous material defining the equivalent complex ENZ response of the metal.

effect to be isolated from the generation of hot electrons at the nanotip.[43] The characteristic current−voltage (I−V) response of a peak (Figure S6a) and valley (Figure S6b) shows good rectification between the AFM nanotip and the sample, with no response measured at a bias of V = 0. By setting the AFM bias to V = 0, we measured the sample response as the input laser was periodically switched on and off. This analysis showed that the current increases at a peak and a valley are practically the same (Figure S6c,d), demonstrating that the flux of hot electrons is essentially negligible in the structure. Figure 5c−f provides further analysis of this process, repeating the experiments of Figure S6 for the same nanostructured sample, but with a 50-nm CQD film. In this case, we observed a significant current enhancement at the peak (Figure 5c,e) compared to the valley (Figure 5d,f). We complemented AFM measurements with transmission electron energy loss spectroscopy (EELS) performed at 1.1 eV (λ = 1127 nm). EELS provides a spatial map with nanometer resolution[44] of the electromagnetic field distribution in our ENZ samples, further showing that electromagnetic radiation is strongly localized in the metallic peak (Figure 7). The AFM + EELS experiments demonstrate that the small ENZ regions formed in proximity to the nanostructured peaks are the mechanism for energy localization and increased absorption of the thin CQD film.

In the next series of experiments, we used PLE measurements to isolate the effects of absorption enhancement in the quantum dot layer. For this characterization, the sample was excited with a range of wavelengths (from 400 to 800 nm) as the relative intensity of the photoluminescence (PL) peak for the CQD film was measured. Figure 8a compares the PLE signal for a 50-nm CQD film deposited on top of a nanostructured Au electrode with varying levels of disorder. We normalized the PLE signal to the PLE value at λ = 530 nm, where the planar sample already shows almost 100% absorption of incoming light. Figure 8a shows a shift of increased relative PLE in the infrared region as a function of increased disorder in the sample. This is directly reflective of the absorption trend in Figure S3, which shows increased infrared absorption when the complex network of ENZ regions is formed. Figure 8b compares the absorption enhancement of our ENZ sample at different CQD film thicknesses. To clearly illustrate the broadband nature of the ENZ enhancement, we normalized the PLE values to that measured at λ = 700 nm, where the nanostructured samples with a 50-nm CQD thickness exhibited the highest absorption increase. For a CQD film of 300 nm, which absorbs almost 100% of visible radiation for wavelengths below 500 nm in a planar configuration, we observed a flat PLE response across the visible and infrared spectrum. This shows that we have effectively enhanced the CQD film absorption efficiency in the infrared range to a level comparable to that in the the visible region, where absorption is almost 100%.

Efficiency Increase in Energy-Harvesting Modules. The ENZ nanostructuring proposed in this work does not require specific photovoltaic cell geometries and can be applied in many different configurations. Although a thorough discussion of this point clearly falls beyond the scope of this article, we provide here a quantitative analysis by characterizing a simple photovoltaic device (Figure 9a). The structure is a colloidal quantum dot solar-energy-harvesting module composed of a bottom electrode made of ENZ nanostructures grown for different exposure times (t = 360 and 600 s) on a glass substrate. On top of the ENZ material, we deposited a 50-nm layer of TiO_2 (treated with $TiCl_4$), followed by a 300-nm-thick film of PbS CQDs, deposited by spin-casting. The module

DOI: 10.1021/acsami.6b13713
ACS Appl. Mater. Interfaces 2017, 9, 5556−5565

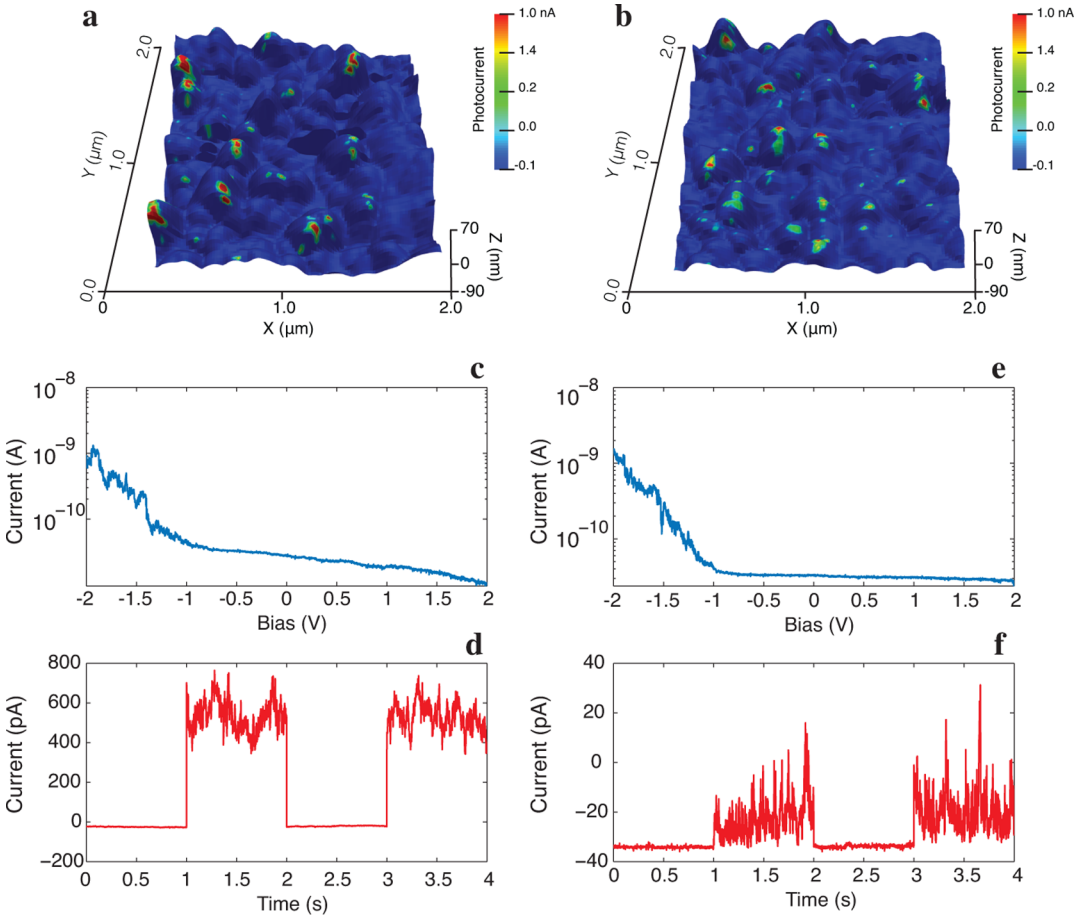

Figure 5. Light trapping in ENZ nanostructures: AFM experimental results. (a,b) Spatial distributions of the photocurrent enhancement (pseudocolor plot) plotted over the surface profile (surface plot) of two different zones in a nanostructured sample with a 10-nm TiO_2 film and a 50-nm CQD film deposited on top. (c,e) Characteristic current−voltage (I−V) responses of (c) a peak region and (e) a valley region. (d,f) Corresponding photocurrents obtained (d) at $V = 0$ and (f) by periodically switching the input laser light at a frequency of 1 Hz. The input laser wavelength was $\lambda = 405$ nm.

was then completed by a 200-nm-thick layer of indium tin oxide (ITO), which acts as a transparent contact in a top-illuminated configuration. Figure 9b shows a transmission electron microscopy (TEM) cross section of a fabricated device. As a reference system, we measured the performances of an identical device whose bottom electrode was made using a planar film of gold with no ENZ.

We collected external quantum efficiency (EQE) spectra under short-circuit conditions and compared the performance of ENZ nanostructures with the quantum efficiency of the planar device with a flat metallic bottom electrode. Figure 9c,d reports the results. In the presence of ENZ nanostructures, the EQE spectra manifested a large broadband enhancement, which was 170% averaged over the absorption bandwidth of the CQDs. In the range between 400 and 600 nm, where the solar spectrum (Figure 9d, solid orange area) has the highest spectral density, the EQE efficiency increase reached values of up to 250%. The efficiency increase was considerably higher (up to 350%) in the infrared region, for wavelengths of $\lambda > 1000$ nm, higher than the excitonic peak of the CQDs located at 980 nm.

Toward a Universal ENZ Nanomaterial. The versatility of electroplating allows the synthesis of ENZ nanomaterials using different metals. Figure 10 summarizes the results obtained by applying electroplating to silver (Figure 10a−c) and palladium (Figure 10d−f) metallic substrates. The use of different metals leads to very different nanostructured surfaces, which exhibit diverse curvatures and, therefore, ENZ regions (Figure 10a,d). The geometric nature of the ENZ regions, however, is expected to lead to a broadband absorption enhancement when a thin layer of CQDs is deposited on top of the metal. Figure 10b,e reports PLE measurements in the visible and near-infrared ranges for planar and nanostructured samples, respectively, and Figure 10c,f shows the corresponding PLE enhancements factors. The CQD thickness in the sample was 50 nm. Despite the different materials used, in all cases, we observed a large and broadband absorption increase in the CQDs that ranged from 200% to 400% at wavelengths between 500 and 900 nm. The ubiquitous observation of this effect shows the possibility of creating universal broadband ENZ nanostructures from cheap metallic materials that can lead to high-performing and low-cost energy-harvesting devices for photocatalysis to photovoltaics. An interesting research direction in this field is also to explore the development of electroplating from semiconductor substrates, which are ideal for industrial optoelectronic applications.

CONCLUSIONS

In this work we introduced a new class of ENZ nanomaterials that harvest white-light energy from the visible to the infrared range of the spectrum in thin CQD films for optoelectronic

DOI: 10.1021/acsami.6b13713
ACS Appl. Mater. Interfaces 2017, 9, 5556−5565

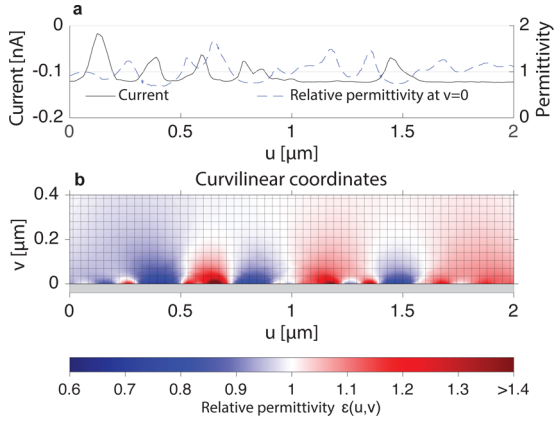

Figure 6. Correlation between ENZ regions and photocurrent enhancement: theory vs AFM experiments. (a) Comparison of the distribution of AFM-measured photocurrent (solid black line) with the refractive index distribution of the ENZ regions in the sample. These calculations were done by first extracting a section from Figure 5 and calculating the equivalent ENZ index representation in the (u, v) space, which is presented in panel b. We then mapped the photocurrent from the original (x, y) coordinates to the ENZ space (u, v), and superimposed the two distributions. This calculation shows a perfect one-to-one correspondence between the occurrence of ENZ regions (minima of the refractive index) and peaks in the photocurrent.

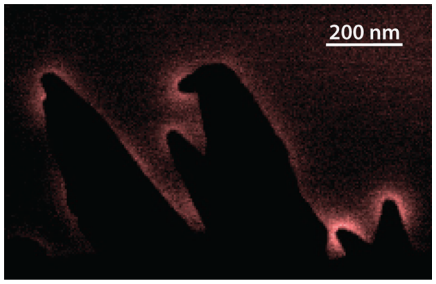

Figure 7. Electron energy loss spectroscopy (EELS) of ENZ samples. Spatial map of the transmission EELS on a disordered sample measured at 1.1 eV. The metallic sample is the black area in the figure.

applications. Our strategy engineers a suitable optical transformation from random metallic materials, obtaining complex ENZ materials with an excellent broadband response. AFM and spatial photoluminescence efficiency measurements confirmed our theoretical models and demonstrated that absorption in active films could be dramatically increased, achieving an almost flat absorption from the visible to the near-infrared region in thin CQD layers. Experiments on an ENZ-based solar-harvesting device performed between λ = 400 nm and λ = 1200 nm reported a fully broadband, 170% quantum efficiency increase when compared to an identical planar structure with no ENZ. The potential impact of this material is indicated by the remarkable value of EQE enhancement obtained with the thin films of CQDs employed in our experiments. The light–matter interaction occurring in the ENZ nanomaterials and reported in this work is a general effect that does not rely on the type of absorptive medium or oxide employed, as illustrated in Figures 4 and 10. This enables the design of new high-performing structures employing inexpensive metals, such as aluminum. The possibility of engineering such a new nanostructured material represents a significant advance in the photonic enhancement of CQD optoelectronics and forms

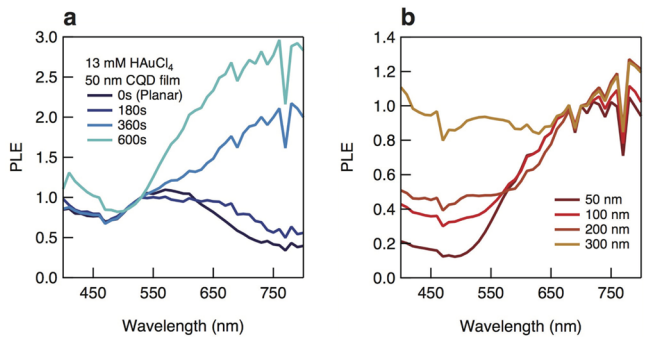

Figure 8. Contribution of the active CQD film. (a) Photoluminescence excitation (PLE) as a function of nanostructuring time for a 50-nm CQD film atop nanostructured Au substrates prepared with 13 mM $HAuCl_4$ solution. (b) Corresponding PLE signals of CQD films (as a function of film thickness) atop nanostructured Au reflectors with a fixed level of nanostructuring time. In panel a, the PLE signal is normalized with respect to the PLE measured at a wavelength of λ = 530 nm, which corresponds to almost 100% of absorption of the planar sample. Conversely, in panel b, the PLE is normalized with respect to the PLE value at λ = 700 nm, which corresponds to the highest enhancement observed in panel a for a CQD layer of 50-nm thickness.

the basis for the development of a new generation of photovoltaic devices with the potential to reach the thermodynamic efficiency limit and completely harvest incoming solar photons.

MATERIALS AND METHODS

Substrate Fabrication: Electrodeposition. Electrodeposition was carried out using an Ivium Technologies CompactStat unit, designed as a portable electrochemical interface and impedance analyzer, with a power configuration of ±30 mA at ±10 V. The electrodeposition procedure employed a four-probe/three-electrode configuration in which the working electrode was connected to the gold- (Au-) coated substrate, the counter electrode was connected to a platinum-coated (Pt) titanium mesh electrode, and the reference electrode was connected to a BASi Ag/AgCl reference electrode (RE-5B with flexible wire connector). Solutions of $HAuCl_4$ were prepared in the following concentrations in 0.5 M HCl stock solution: 13, 26, and 40 mM $HAuCl_4$. Electrodeposition was carried out between 180 and 600 s and measured currents varied from approximately −2 to −9 mA depending on the $HAuCl_4$ concentration.

CQD Film Fabrication. PbS quantum dots (synthesized and exchanged following previously published protocols[45]) were deposited at a concentration of 50 mg/mL in octane through a 0.2-μm filter and were then subjected to solid-state exchange using 3-mercaptopropionic acid at a concentration of 1% v/v in methanol or tetrabutylammonium iodide (TBAI) at a concentration of 10 mg/mL in methanol. Finally, the film was rinsed twice with pure methanol. All samples were spin-casted at 2500 rpm.

Spectrophotometer Measurements. All absorption measurements were carried out using a Perkin-Elmer Lambda 950 UV–vis–NIR spectrophotometer equipped with an integrating sphere. Samples were placed at the center of the integrated sphere tilted at an angle of 20° relative to the incident beam. The total transmission (T) and reflectance (R) were collected by the integrating sphere detector with all ports closed except the one for the incident beam. Absorption was calculated as 100% − T − R. The 100% transmission baseline measurement was an empty sphere.

Photoluminescence Excitation. Photoluminescence excitation was carried out using a Horiba Fluorolog spectrofluorometer. Samples were place in the testing chamber at an angle of 30 degree with respect to the excitation signal, with the detector chamber at 90 deg from the excitation chamber. Photoluminescence from PbS films was measured

DOI: 10.1021/acsami.6b13713
ACS Appl. Mater. Interfaces 2017, 9, 5556–5565

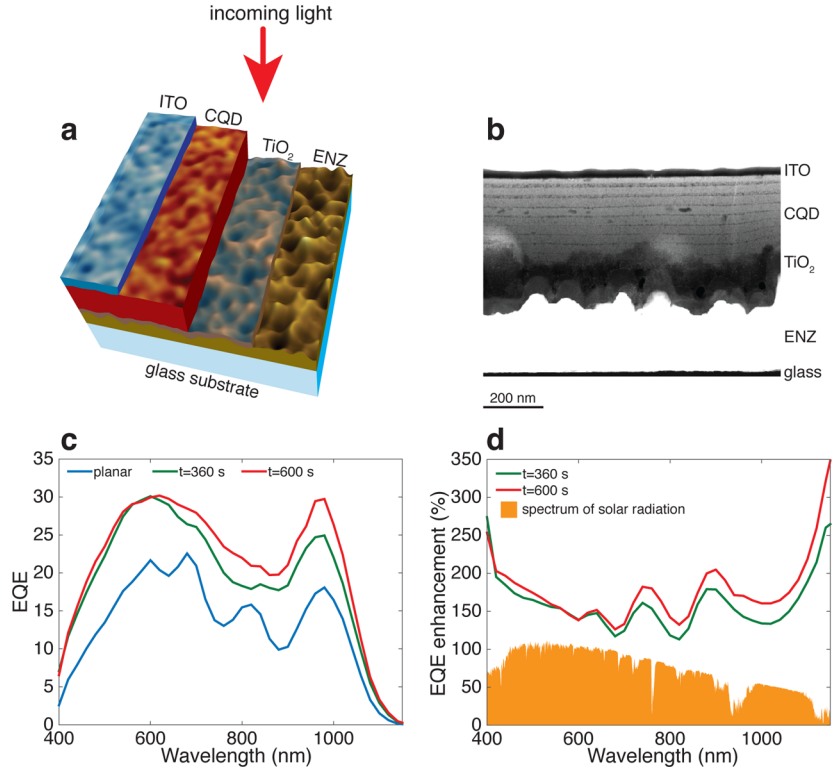

Figure 9. Performance increase of an ENZ-based solar harvesting device versus a planar module with no ENZ structures. (a) Three-dimensional sketch of a harvesting module comprising a bottom electrode made of ENZ nanostructures, with a 50-nm layer of TiO_2 deposited on top, followed by 300 nm of CQDs and completed by indium tin oxide (ITO). (b) Transmission electron microscopy (TEM) cross section of a fabricated sample, with ENZ nanostructures prepared with an exposure time of t = 360 s. (c,d) External quantum efficiency spectra measured at visible and near-infrared wavelengths (from 400 to 1200 nm).

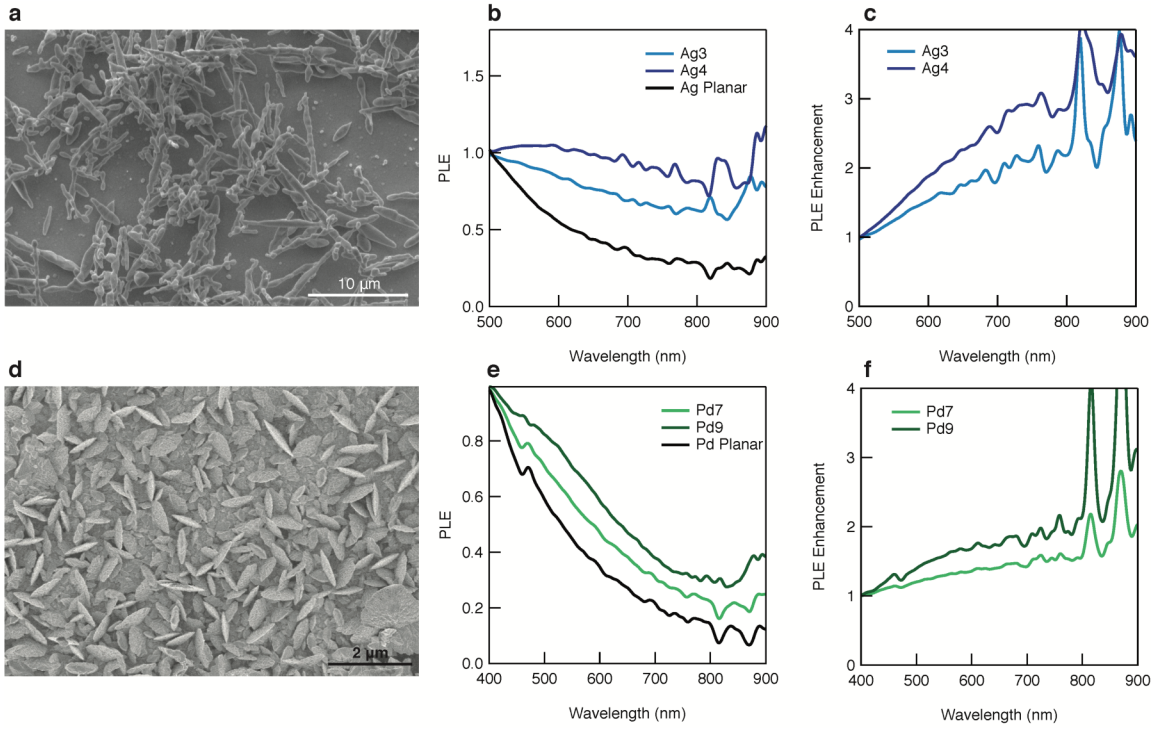

Figure 10. Enhanced absorption of CQDs deposited on ENZ generated on (a–c) silver and (d–f) palladium substrates. (a,d) SEM images of nanostructured electrodes created by using (a) silver and (d) palladium metallic substrates. (b,e) PLE signals when a 50-nm-thick CQD layer was deposited on top of the metallic structures. (c,f) Corresponding broadband enhancements in the visible and near-infrared regions.

DOI: 10.1021/acsami.6b13713
ACS Appl. Mater. Interfaces 2017, 9, 5556–5565

in this chamber. The spectrum of 400−800 nm (in 10-nm increments) was used to excite the film, while the detector was configured to measure the PL signal at 1050−1100 nm (based on the intensity peak for the given sample), yielding a relative PL intensity as a function of excitation wavelength

Scanning Electron Microscopy. Scanning electron microscopy images were obtained using an FEI Quanta FEG 250 environmental SEM/STEM (scanning transmission electron microscopy) instrument. All top-view images were obtained using a 45° tilted holder to highlight surface texture. Images were obtained using 5, 10, and 20 keV based on the application and generally magnified to the order of 1−10 μm depending on the application.

Atomic Force Microscopy. Photoconductive atomic force microscopy, including topography measurements, was performed on an Asylum Research Cypher AFM instrument, using 2 N/m Ti/Ir-coated Si ultrasharp tips from Asylum. A 405-nm laser beam, with 1 mW optical power, was used to illuminate the sample. Laser light was conditioned through a microscope objective to form a 3-μm-diameter spot on the active layer of the sample. To avoid electric shorts between the ultrasharp AFM tips and the nanostructured metal, we use atomic layer deposition (ALD) to deposit conformally a 10-nm layer of amorphous TiO_2 atop the metal surface. The TiO_2 layer forms a rectifying junction with the quantum dots with no effect on the ENZ in the quantum dot film, because of the negligible absorption of TiO_2 at visible and infrared frequencies.

EELS Measurements. Electron energy-loss spectroscopy was performed on an FEI 60−300 kV Titan spectrometere with monochromator and spherical aberration corrector at 200 kV. Disordered samples were prepared by applying a voltage bias of $V = -0.3$ V with 1.5−2 cm separation of between the Pt counter electrode and Au working electrode. Electrodeposition was carried out for 300 s in 100 mM $HAuCl_4$ solution. Disordered samples were sonicated in 10 mL of ethanol solution for 20 min. We then deposited 2 mL of solution on a transmission electron microscopy (TEM) copper grid for the EELS analysis.

■ ASSOCIATED CONTENT

Supporting Information

The Supporting Information is available free of charge on the ACS Publications website at DOI: 10.1021/acsami.6b13713.

Movie showing light splitting in complex ENZ structures as calculated from first-principles simulations (AVI)

Discussion of transformation optics, example of conformal mapping by nonlinear grid dynamics, spatial distribution of epsilon-near-zero regions in the original space, experimental absorption of nanostructured ENZ materials, FDTD-simulated dispersion curve of Au, absorption of ENZ regions of different lengths, and experimental AFM photocurrent measurements of nanostructured electrodes with no CQDs deposited on top (PDF)

■ AUTHOR INFORMATION

Corresponding Authors

*E-mail: ted.sargent@utoronto.ca.

*E-mail: andrea.fratalocchi@kaust.edu.sa.

ORCID

S. O. Kelley: 0000-0003-3360-5359

A. Fratalocchi: 0000-0001-6769-4439

Author Contributions

‡A.J.L., M.B., and Y.T. contributed equally to the preparation of the manuscript

Notes

The authors declare no competing financial interest.

■ ACKNOWLEDGMENTS

For computer time, we used the resources of the KAUST Supercomputing Laboratory and the Redragon cluster of the Primalight group. A.F. acknowledges funding from KAUST (Award CRG-1-2012-FRA-005). E.H.S. acknowledges funding from the Ontario Research Fund.

■ REFERENCES

(1) Oertel, D. C.; Bawendi, M. G.; Arango, A. C.; Bulović, V. Photodetectors based on Treated CdSe Quantum-Dot Films. *Appl. Phys. Lett.* **2005**, *87*, 213505−3.

(2) Clifford, J. P.; Konstantatos, G.; Johnston, K. W.; Hoogland, S.; Levina, L.; Sargent, E. H. Fast, Sensitive and Spectrally Tunable Colloidal-Quantum-Dot Photodetectors. *Nat. Nanotechnol.* **2009**, *4*, 40−44.

(3) Konstantatos, G.; Howard, I.; Fischer, A.; Hoogland, S.; Clifford, J.; Klem, E.; Levina, L.; Sargent, E. H. Ultrasensitive Solution-Cast Quantum Dot Photodetectors. *Nature* **2006**, *442*, 180−183.

(4) Konstantatos, G.; Badioli, M.; Gaudreau, L.; Osmond, J.; Bernechea, M.; de Arquer, F. P. G.; Gatti, F.; Koppens, F. H. L. Hybrid Graphene-Quantum Dot Phototransistors with Ultrahigh Gain. *Nat. Nanotechnol.* **2012**, *7*, 363−368.

(5) Chuang, C.-H. M.; Brown, P. R.; Bulović, V.; Bawendi, M. G. Improved Performance and Stability in Quantum Dot Solar Cells through Band Alignment Engineering. *Nat. Mater.* **2014**, *13*, 796−801.

(6) Ip, A. H.; Thon, S. M.; Hoogland, S.; Voznyy, O.; Zhitomirsky, D.; Debnath, R.; Levina, L.; Rollny, L. R.; Carey, G. H.; Fischer, A.; Kemp, K. W.; Kramer, I. J.; Ning, Z.; Labelle, A. J.; Chou, K. W.; Amassian, A.; Sargent, E. H. Hybrid Passivated Colloidal Quantum Dot Solids. *Nat. Nanotechnol.* **2012**, *7*, 577−582.

(7) Rath, A. K.; Bernechea, M.; Martinez, L.; de Arquer, F. P. G.; Osmond, J.; Konstantatos, G. Solution-processed Inorganic Bulk Nano-Heterojunctions and their Application to Solar Cells. *Nat. Photonics* **2012**, *6*, 529−534.

(8) Choi, J. J.; Wenger, W. N.; Hoffman, R. S.; Lim, Y.-F.; Luria, J.; Jasieniak, J.; Marohn, J. A.; Hanrath, T. Solution-Processed Nanocrystal Quantum Dot Tandem Solar Cells. *Adv. Mater.* **2011**, *23*, 3144−3148.

(9) Pattantyus-Abraham, A. G.; Kramer, I. J.; Barkhouse, A. R.; Wang, X.; Konstantatos, G.; Debnath, R.; Levina, L.; Raabe, I.; Nazeeruddin, M. K.; Grätzel, M.; Sargent, E. H. Depleted-Heterojunction Colloidal Quantum Dot Solar Cells. *ACS Nano* **2010**, *4*, 3374−3380.

(10) Jean, J.; Chang, S.; Brown, P. R.; Cheng, J. J.; Rekemeyer, P. H.; Bawendi, M. G.; Gradecak, S.; Bulović, V. ZnO Nanowire Arrays for Enhanced Photocurrent in PbS Quantum Dot Solar Cells. *Adv. Mater.* **2013**, *25*, 2790−2796.

(11) Adinolfi, V.; Kramer, I. J.; Labelle, A. J.; Sutherland, B. R.; Hoogland, S.; Sargent, E. H. Photojunction Field-Effect Transistor Based on a Colloidal Quantum Dot Absorber Channel Layer. *ACS Nano* **2015**, *9*, 356−362.

(12) Labelle, A. J.; Thon, S. M.; Kim, J. Y.; Lan, X.; Zhitomirsky, D.; Kemp, K. W.; Sargent, E. H. Conformal Fabrication of Colloidal Quantum Dot Solids for Optically Enhanced Photovoltaics. *ACS Nano* **2015**, *9*, 5447−5453.

(13) Barkhouse, D. A. R.; Debnath, R.; Kramer, I. J.; Zhitomirsky, D.; Pattantyus-Abraham, A. G.; Levina, L.; Etgar, L.; Grätzel, M.; Sargent, E. H. Depleted Bulk Heterojunction Colloidal Quantum Dot Photovoltaics. *Adv. Mater.* **2011**, *23*, 3134−3138.

(14) Lan, X.; Bai, J.; Masala, S.; Thon, S. M.; Ren, Y.; Kramer, I. J.; Hoogland, S.; Simchi, A.; Koleilat, G. I.; Paz-Soldan, D.; Ning, Z.; Labelle, A. J.; Kim, J. Y.; Jabbour, G.; Sargent, E. H. Self-Assembled, Nanowire Network Electrodes for Depleted Bulk Heterojunction Solar Cells. *Adv. Mater.* **2013**, *25*, 1769−1773.

(15) Kramer, I. J.; Zhitomirsky, D.; Bass, J. D.; Rice, P. M.; Topuria, T.; Krupp, L.; Thon, S. M.; Ip, A. H.; Debnath, R.; Kim, H.-C.; Sargent, E. H. Ordered Nanopillar Structured Electrodes for Depleted Bulk Heterojunction Colloidal Quantum Dot Solar Cells. *Adv. Mater.* **2012**, *24*, 2315−2319.

DOI: 10.1021/acsami.6b13713
ACS Appl. Mater. Interfaces 2017, 9, 5556−5565

(16) Adachi, M. M.; Labelle, A. J.; Thon, S. M.; Lan, X.; Hoogland, S.; Sargent, E. H. Broadband Solar Absorption Enhancement via Periodic Nanostructuring of Electrodes. *Sci. Rep.* **2013**, *3*, 2928.
(17) Labelle, A. J.; Thon, S. M.; Masala, S.; Adachi, M. M.; Dong, H.; Ip, A. H.; Farahani, M.; Fratalocchi, A.; Sargent, E. H. Colloidal Quantum Dot Solar Cells Exploiting Hierarchical Structuring. *Nano Lett.* **2015**, *15*, 1101−1108.
(18) Atwater, H. A.; Polman, A. Plasmonics for Improved Photovoltaic Devices. *Nat. Mater.* **2010**, *9*, 205−213.
(19) Neumann, O.; Feronti, C.; Neumann, A. D.; Dong, A.; Schell, K.; Lue, B.; Kim, E.; Quinn, M.; Thompson, S.; Grady, N.; Nordlander, P.; Oden, M.; Halas, N. J. Compact Solar Autoclave Based on Steam Generation using Broadband Light-Harvesting Nanoparticles. *Proc. Natl. Acad. Sci. U. S. A.* **2013**, *110*, 11677−11681.
(20) Neumann, O.; Urban, A.; Day, J.; Lal, S.; Nordlander, P.; Halas, N. J. Solar Vapor Generation Enabled by Nanoparticles. *ACS Nano* **2013**, *7*, 42−49.
(21) Mukherjee, S.; Libisch, F.; Large, N.; Neumann, O.; Brown, L. V.; Cheng, J.; Lassiter, J. B.; Carter, E. A.; Nordlander, P.; Halas, N. J. Hot Electrons Do the Impossible: Plasmon-Induced Dissociation of H2 on Au. *Nano Lett.* **2013**, *13*, 240−247.
(22) Paz-Soldan, D.; Lee, A.; Thon, S. M.; Adachi, M. M.; Dong, H.; Maraghechi, P.; Yuan, M.; Labelle, A. J.; Hoogland, S.; Liu, K.; Kumacheva, E.; Sargent, E. H. Jointly Tuned Plasmonic-Excitonic Photovoltaics Using Nanoshells. *Nano Lett.* **2013**, *13*, 1502−1508.
(23) Shockley, W.; Queisser, H. J. Detailed Balance Limit of Efficiency of p-n Junction Solar Cells. *J. Appl. Phys.* **1961**, *32*, 510−519.
(24) Silveirinha, M.; Engheta, N. Tunneling of Electromagnetic Energy through Subwavelength Channels and Bends using Epsilon-Near-Zero Materials. *Phys. Rev. Lett.* **2006**, *97*, 157403.
(25) Maas, R.; Parsons, J.; Engheta, N.; Polman, A. Experimental Realization of an Epsilon-near-Zero Metamaterial at Visible Wavelengths. *Nat. Photonics* **2013**, *7*, 907−912.
(26) Vesseur, E. J. R.; Coenen, T.; Caglayan, H.; Engheta, N.; Polman, A. Experimental Verification of $n = 0$ Structures for Visible Light. *Phys. Rev. Lett.* **2013**, *110*, 013902.
(27) Liu, C.; Di Falco, A.; Molinari, D.; Khan, Y.; Ooi, B.; Krauss, T.; Fratalocchi, A. Enhanced Energy Storage in Chaotic Optical Resonators. *Nat. Photonics* **2013**, *7*, 473−478.
(28) Conti, C.; Leonetti, M.; Fratalocchi, A.; Angelani, L.; Ruocco, G. Condensation in Disordered Lasers: Theory, Simulations, and Experiments. *Phys. Rev. Lett.* **2008**, *101* (4), 143901.
(29) Liu, C.; van der Wel, R. E. C.; Rotenberg, N.; Kuipers, L.; Krauss, T. F.; Di Falco, A.; Fratalocchi, A. Triggering Extreme Events at the Nanoscale in Photonic Seas. *Nat. Phys.* **2015**, *11*, 358−363.
(30) Conti, C.; Fratalocchi, A. Dynamic Light Diffusion, Three-dimensional Anderson Localization and Lasing in Inverted Opals. *Nat. Phys.* **2008**, *4*, 794−798.
(31) Stockman, M. I. Chaos and Spatial Correlations for Dipolar Eigenproblems. *Phys. Rev. Lett.* **1997**, *79*, 4562−4565.
(32) Shalaev, V. M. *Nonlinear Optics of Random Media: Fractal Composites and Metal-Dielectric Films*; Springer: Berlin, 2013.
(33) Huang, J.; Liu, C.; Zhu, Y.; Masala, S.; Alarousu, E.; Han, Y.; Fratalocchi, A. Harnessing Structural Darkness in the Visible and Infrared Wavelengths for a New Source of Light. *Nat. Nanotechnol.* **2016**, *11*, 60−66.
(34) Soleymani, L.; Fang, Z.; Lam, B.; Bin, X.; Vasilyeva, E.; Ross, A. J.; Sargent, E. H.; Kelley, S. O. Hierarchical Nanotextured Microelectrodes Overcome the Molecular Transport Barrier To Achieve Rapid, Direct Bacterial Detection. *ACS Nano* **2011**, *5*, 3360−3366.
(35) Vasilyeva, E.; Lam, B.; Fang, Z.; Minden, M. D.; Sargent, E. H.; Kelley, S. O. Direct Genetic Analysis of Ten Cancer Cells: Tuning Sensor Structure and Molecular Probe Design for Efficient mRNA Capture. *Angew. Chem., Int. Ed.* **2011**, *50*, 4137−4141.
(36) Ivanov, I.; Stojcic, J.; Stanimirovic, A.; Sargent, E.; Nam, R. K.; Kelley, S. O. Chip-based Nanostructured Sensors Enable Accurate Identification and Classification of Circulating Tumor Cells in Prostate Cancer Patient Blood Samples. *Anal. Chem.* **2013**, *85*, 398−403.
(37) Lam, B.; Das, J.; Holmes, R. D.; Live, L.; Sage, A.; Sargent, E. H.; Kelley, S. O. Solution-Based Circuits Enable Rapid and Multiplexed Pathogen Detection. *Nat. Commun.* **2013**, *4*, 2001.
(38) Maier, S. *Plasmonics: Fundamentals and Applications*; Springer: New York, 2007.
(39) Leonhardt, U. Optical Conformal Mapping. *Science* **2006**, *312*, 1777−1780.
(40) Pendry, J.; Aubry, A.; Smith, D.; Maier, S. Transformation Optics and Subwavelength Control of light. *Science* **2012**, *337*, 549−552.
(41) Totero Gongora, J.; Miroshnichenko, A.; Kivshar, Y.; Fratalocchi, A. Energy Equipartition and Unidirectional Emission in a Spaser Nanolaser. *Laser and Photonics Rev.* **2016**, *10*, 432−440.
(42) Adachi, S. *The Handbook on Optical Constants of Metals: In Tables and Figures*; World Scientific: Singapore, 2012.
(43) Giugni, A.; Torre, B.; Toma, A.; Francardi, M.; Malerba, M.; Alabastri, A.; Proietti Zaccaria, R.; Stockman, M. I.; Di Fabrizio, E. Hot-Electron Nanoscopy Using Adiabatic Compression of Surface Plasmons. *Nat. Nanotechnol.* **2013**, *8*, 845−852.
(44) Egerton, R. F. Electron Energy-loss Spectroscopy in the TEM. *Rep. Prog. Phys.* **2009**, *72*, 016502.
(45) Ip, H. A.; Thon, S. M.; Hoogland, S.; Voznyy, O.; Zhitomirsky, D.; Debnath, R.; Levina, L.; Rollny, L. R.; Carey, G. H.; Fischer, A.; Kemp, K. W.; Kramer, I. J.; Ning, Z.; Labelle, A. J.; Chou, K. W.; Amassian, A.; Sargent, E. H. Hybrid Passivated Colloidal Quantum Dot Solids. *Nat. Nanotechnol.* **2012**, *7*, 577−582.

DOI: 10.1021/acsami.6b13713
ACS Appl. Mater. Interfaces 2017, 9, 5556−5565